

New Hybrid Runge–Kutta Methods for Unsteady Reactive Flow Simulation: Applications

Jack J. Yoh*

Lawrence Livermore National Laboratory, Livermore, California 94551

and

Xiaolin Zhong†

University of California, Los Angeles, Los Angeles, California 90095

The applicability is examined of the new hybrid Runge–Kutta methods derived in the companion paper (Yoh, J. J., and Zhong, X., “New Hybrid Runge–Kutta Methods for Unsteady Reactive Flow Simulation,” *AIAA Journal*, Vol. 42, No. 8, 2004, pp. 1593–1600) by specifically analyzing both nonstiff and stiff system of equations that represent multidimensional reactive flows. In a reactive flow simulation, the standard explicit calculation is prohibitively expensive because of the small time steps needed to address the stiffness of a governing differential system. The new hybrid Runge–Kutta schemes are suitable for this task because the time-step size is controlled by the Courant condition, whereas the stiffness is treated by an unconditionally stable method. This set of methods also meets the modern computing needs of high-order accuracy and low-storage requirement. A representative scheme is used to simulate a series of combustion problems that include model equations with stiff sources and multidimensional detonations with complex chemical kinetics.

Introduction

THIS paper is the second of two papers that describe high-order hybrid Runge–Kutta methods intended for simulating transient reacting flows. Such methods are necessary when the governing system of differential equations has both nonstiff and stiff elements that can be treated by two different solvers, namely, a nonstiff and a stiff solver. For instance, arrays f and g in the following equation may represent the two solvers whose time-step size is determined solely by the stability criteria for a nonstiff solver, f , for example,

$$\frac{du}{dt} = f(u, t) + g(u, t) \quad (1)$$

In the companion paper,¹ we developed a set of semi-implicit Runge–Kutta (SIRK) schemes that combines an explicit Runge–Kutta scheme and an implicit Runge–Kutta scheme in a manner that allows the time-step size to be determined solely by the Courant condition. In this paper, we illustrate the strengths of the new hybrid methods through a series of calculations of model reactive flow systems.

For direct numerical simulation of transients induced by shocks, detonations, or any type of loading with a broad frequency range, third-order or higher methods are desirable to capture the short timescale events that take place in these dynamic flowfields. Most of methods in the literature share the common drawback that their temporal accuracy is of a low order. To achieve high-order accuracy with a good stability property that exceeds the unconditional stability of fully implicit methods, we have creatively coupled the explicit and implicit methods in a way that allows for controlling the time step independent of stiffness of the system and for maintaining the high-order numerical accuracy and efficiency of the underlying

single-step scheme. Presentations of several noted benefits of the new hybrid schemes are the main focus of this paper. For further algorithmic discussions, readers are referred to the companion paper.¹

In the first section, high-order SIRK algorithms for integrating Eq. (1) are given. The general SIRK methods are labeled SIRK-3 and SIRK-4 for autonomous and nonautonomous versions, respectively. The low-storage (LS) version is noted, LSSIRK-4A and LSSIRK-4C for the kind of implicit solver used. (See Ref. 1 for more detail.) In sections to follow, new algorithms are tested for numerical accuracy. A set of model equations is considered to reflect the stability property and high-order accuracy of the new schemes. The paper will conclude by presenting extensive applications of the new hybrid methods in reacting flow simulations such as multidimensional detonation calculations.

Numerical Methods

In numerical computations of reacting flows using the method of lines, spatial derivatives in the governing partial differential equations are first approximated by using a spatial discretization scheme. The spatial discretization leads to a system of first-order differential equations in the form of Eq. (1). For systems with a time-dependent forcing term or boundary condition, Eq. (1) is not autonomous, that is, $f(t, u)$ and $g(t, u)$ are explicit functions of time. In the hybrid, that is, explicit/implicit, Runge–Kutta framework, array $g(t, u)$ contains the stiff source terms and some spatial discretizations of diffusive operators, for instance. The remaining nonstiff terms are assigned to array $f(t, u)$. The splitting of stiff and nonstiff terms in Eq. (1) makes it possible to solve the equation by a SIRK scheme,¹ which is a one-step method involving intermediate stages to achieve high-order accuracy and good stability properties.

A general r -stage SIRK method integrates Eq. (1) by simultaneously treating f explicitly and g implicitly. Two versions of SIRK methods, derived in Ref. 1, are denoted method A and method C. For r -stage schemes, SIRK- r A or SIRK- r C represent two families of methods that are r stage.

The SIRK- r A method is written in the following form:

$$u^{n+1} = u^n + \sum_{j=1}^r w_j k_j \quad (2)$$

Received 14 July 2003; revision received 25 March 2004; accepted for publication 29 March 2004. Copyright © 2004 by the American Institute of Aeronautics and Astronautics, Inc. All rights reserved. Copies of this paper may be made for personal or internal use, on condition that the copier pay the \$10.00 per-copy fee to the Copyright Clearance Center, Inc., 222 Rosewood Drive, Danvers, MA 01923; include the code 0001-1452/04 \$10.00 in correspondence with the CCC.

*Staff Scientist, Energetic Materials Center, P.O. Box 808, L-268; yoh1@llnl.gov. Member AIAA.

†Professor, Mechanical and Aerospace Engineering Department. Associate Fellow AIAA.

$$\begin{aligned}
\mathbf{k}_i &= h\mathbf{f}\left(t_n + r_i h, \mathbf{u}^n + \sum_{j=1}^{i-1} b_{ij}\mathbf{k}_j\right) \\
&\quad + h\mathbf{g}\left(t_n + s_i h, \mathbf{u}^n + \sum_{j=1}^{i-1} c_{ij}\mathbf{k}_j + d_i\mathbf{k}_i\right) \\
&\quad (i = 1, \dots, r) \quad (3)
\end{aligned}$$

where h is the time step size.

Unlike the first, the SIRK- r C method makes use of the linearized implicit term \mathbf{g} to obtain r -stage SIRK method in the following manner:

$$\mathbf{u}^{n+1} = \mathbf{u}^n + \sum_{j=1}^r w_j \mathbf{k}_j \quad (4)$$

$$\begin{aligned}
&\left[\mathbf{I} - h d_i \mathbf{J}\left(t_n + s_i h, \mathbf{u}^n + \sum_{j=1}^{i-1} c_{ij}\mathbf{k}_j\right) \right] \mathbf{k}_i \\
&= h \left[\mathbf{f}\left(t_n + r_i h, \mathbf{u}^n + \sum_{j=1}^{i-1} b_{ij}\mathbf{k}_j\right) \right. \\
&\quad \left. + \mathbf{g}\left(t_n + s_i h, \mathbf{u}^n + \sum_{j=1}^{i-1} c_{ij}\mathbf{k}_j\right) \right], \quad (i = 1, \dots, r) \quad (5)
\end{aligned}$$

where $\mathbf{J} = \partial \mathbf{g} / \partial \mathbf{u}$ is the Jacobian matrix of the stiff term \mathbf{g} .

In the companion paper, we showed that four stages are required to construct a third-order accurate SIRK schemes in general. In the two families of schemes just shown, a significant memory storage is required to operate with four stages and $5N$ locations, where N represents the number of governing variables. This storage requirement is too restrictive when computing multidimensional reactive flows. A family of LS versions that require no more than $2N$ storage locations is listed next. Like the generalSIRK schemes, the LS versions are derived from the same accuracy and L -stability conditions. Two versions, LSSIRK-4A and LSSIRK-4C, once again are described here. For detailed discussions, readers are referred to the companion paper.¹

The fully expanded third-order LSSIRK-4A scheme is

$$\begin{aligned}
\mathbf{k}_1 &= h[\mathbf{f}(t_0, \mathbf{u}_0) + \mathbf{g}(t_0 + s_1 h, \mathbf{u}_0 + c_1 \mathbf{k}_1)] \\
\mathbf{u}_1 &= \mathbf{u}_0 + b_1 \mathbf{k}_1 \\
\mathbf{k}_2 &= a_2 \mathbf{k}_1 + h[\mathbf{f}(t_0 + r_2 h, \mathbf{u}_1) + \mathbf{g}(t_0 + s_2 h, \mathbf{u}_1 + \bar{c}_2 \mathbf{k}_1 + c_2 \mathbf{k}_2)] \\
\mathbf{u}_2 &= \mathbf{u}_1 + b_2 \mathbf{k}_2 \\
\mathbf{k}_3 &= a_3 \mathbf{k}_2 + h[\mathbf{f}(t_0 + r_3 h, \mathbf{u}_2) + \mathbf{g}(t_0 + s_3 h, \mathbf{u}_2 + \bar{c}_3 \mathbf{k}_2 + c_3 \mathbf{k}_3)] \\
\mathbf{u}_3 &= \mathbf{u}_2 + b_3 \mathbf{k}_3 \\
\mathbf{k}_4 &= a_4 \mathbf{k}_3 + h[\mathbf{f}(t_0 + r_4 h, \mathbf{u}_3) + \mathbf{g}(t_0 + s_4 h, \mathbf{u}_3 + \bar{c}_4 \mathbf{k}_3 + c_4 \mathbf{k}_4)] \\
\mathbf{u}_4 &= \mathbf{u}_3 + b_4 \mathbf{k}_4 \quad (6)
\end{aligned}$$

Similarly, the third-order LSSIRK-4C scheme is

$$\begin{aligned}
&[\mathbf{I} - h c_1 \mathbf{J}(t_0 + s_1 h, \mathbf{u}_0)] \mathbf{k}_1 = h[\mathbf{f}(t_0, \mathbf{u}_0) + \mathbf{g}(t_0 + s_1 h, \mathbf{u}_0)] \\
\mathbf{u}_1 &= \mathbf{u}_0 + b_1 \mathbf{k}_1 \\
&[\mathbf{I} - h c_2 \mathbf{J}(t_0 + s_2 h, \mathbf{u}_1 + \bar{c}_2 \mathbf{k}_1)] \mathbf{k}_2 = h[\mathbf{f}(t_0 + r_2 h, \mathbf{u}_1) \\
&\quad + \mathbf{g}(t_0 + s_2 h, \mathbf{u}_1 + \bar{c}_2 \mathbf{k}_1)] \\
&\quad + a_2 [\mathbf{I} - h c_2 \mathbf{J}(t_0 + s_2 h, \mathbf{u}_1 + \bar{c}_2 \mathbf{k}_1)] \mathbf{k}_1 \\
\mathbf{u}_2 &= \mathbf{u}_1 + b_2 \mathbf{k}_2
\end{aligned}$$

$$\begin{aligned}
&[\mathbf{I} - h c_3 \mathbf{J}(t_0 + s_3 h, \mathbf{u}_2 + \bar{c}_3 \mathbf{k}_2)] \mathbf{k}_3 = h[\mathbf{f}(t_0 + r_3 h, \mathbf{u}_2) \\
&\quad + \mathbf{g}(t_0 + s_3 h, \mathbf{u}_2 + \bar{c}_3 \mathbf{k}_2)] \\
&\quad + a_3 [\mathbf{I} - h c_3 \mathbf{J}(t_0 + s_3 h, \mathbf{u}_2 + \bar{c}_3 \mathbf{k}_2)] \mathbf{k}_2 \\
\mathbf{u}_3 &= \mathbf{u}_2 + b_3 \mathbf{k}_3 \\
&[\mathbf{I} - h c_4 \mathbf{J}(t_0 + s_4 h, \mathbf{u}_3 + \bar{c}_4 \mathbf{k}_3)] \mathbf{k}_4 = h[\mathbf{f}(t_0 + r_4 h, \mathbf{u}_3) \\
&\quad + \mathbf{g}(t_0 + s_4 h, \mathbf{u}_3 + \bar{c}_4 \mathbf{k}_3)] \\
&\quad + a_4 [\mathbf{I} - h c_4 \mathbf{J}(t_0 + s_4 h, \mathbf{u}_3 + \bar{c}_4 \mathbf{k}_3)] \mathbf{k}_3 \\
\mathbf{u}_4 &= \mathbf{u}_3 + b_4 \mathbf{k}_4 \quad (7)
\end{aligned}$$

Unlike SIRK-4A and SIRK-4C methods, the LS versions presented here require just the memory locations for \mathbf{k}_j and \mathbf{u}_j at each of four stages used to advance one time step. The coefficients of these schemes are reported in the companion paper.¹

Numerical Simulations

In this section, we validate the accuracy and test the robustness of the new hybrid schemes through a series of model problems. The presented results are calculated by the two linearized methods from each family of schemes, namely, methods C from LSSIRK and SIRK.

Temporal Accuracy Tests

Nonautonomous Ordinary Differential Equations

The first step involves solving the following equation using both implicit and its explicit counterparts of the new scheme:

$$\frac{\partial \mathbf{u}}{\partial t} = \mathbf{A} \mathbf{u} + \mathbf{f}(t) \quad (8)$$

where

$$\mathbf{A} = \begin{bmatrix} 0 & 1 & 0 \\ 0 & 0 & 1 \\ -2 & -5 & -4 \end{bmatrix}, \quad \mathbf{f} = \begin{bmatrix} 0 \\ 0 \\ -4 \sin(t) - 2 \cos(t) \end{bmatrix} \quad (9)$$

The initial condition is $\mathbf{u}(t=0) = \{1, 0, -1\}$. The exact solution of the first component of the equations is $u_{\text{ex}} = \cos(t)$. The temporal accuracy of the SIRK schemes are evaluated by computing the numerical errors of the solutions for a given time step h . A scheme of p th order is expected to satisfy the parameter R_p defined by

$$R_p = e_h / e_{h/2} = 2^p \quad (10)$$

where $e_h = u_{\text{ex}} - u_h$ is the numerical error computed using the time-step size h .

Tables 1 and 2 show a temporal grid refinement study of the third-order LSSIRK schemes, LSSIRK-4A and LSSIRK-4C, for solving Eq. (8). We test the accuracy of the new schemes by solving the same equation once using only the implicit solver and again by the explicit solver. Results in Tables 1 and 2 show that both the implicit Runge–Kutta methods and its explicit counterpart implemented in this new scheme are third-order accurate.

Table 1 Temporal accuracy of the LSSIRK-4A and LSSIRK-4C methods for implicit calculations

Δt	LSSIRK-4A		LSSIRK-4C	
	e_3	R_3	e_3	R_3
$h = 0.0625$	$4.47E-4$	4.9	$8.32E-5$	7.2
$h/2$	$7.04E-5$	6.4	$1.10E-5$	7.5
$h/4$	$9.71E-6$	7.3	$1.42E-6$	7.8
$h/8$	$1.26E-6$	7.7	$1.80E-7$	7.9
$h/16$	$1.60E-7$	7.9	$2.27E-8$	7.9
$h/32$	$2.02E-8$	7.9	$2.84E-9$	8.0
$h/64$	$2.53E-9$	8.0	$3.56E-10$	8.0

Nonautonomous Convection–Diffusion Equation

We consider the following linear convection–diffusion equation:

$$\frac{\partial u}{\partial t} + \frac{\partial u}{\partial x} + \frac{\partial u}{\partial y} = \frac{1}{R} \frac{\partial^2 u}{\partial y^2} + G(x, y, t) \quad (11)$$

where

$$G(x, y, t) = C \exp(Ry/2) \sin(n\pi y) \exp[ik(x - t)] \times \exp(-\alpha_n t) \cos(t) \quad (12)$$

with $\alpha_n = (R/4)[1 + (2n\pi/R)^2]$. The boundary conditions are $u(x, 0) = u(x, 1) = 0$. This equation has both convection and diffusion terms, where the parameter R determines their relative magnitudes. The exact solution of the equation is

$$u_n = C \exp(Ry/2) \sin(n\pi y) \exp[ik(x - t)] \exp(-\alpha_n t) [1 + \sin(t)] \quad (13)$$

if the initial condition is given by the same formula with t set to zero. When R is large, there is a thin diffusion layer on the upper wall with large gradients in the y direction. This makes the differential equation stiff. When the equation is split into the stiff terms of the y directional gradients and the rest of the nonstiff terms, the presented stiff equation can be efficiently and accurately solved by a third-order LS Runge–Kutta scheme.

The equations are computed in a rectangular domain of $0 \leq x \leq 2\pi/k$ and $0 \leq y \leq 1$, using a uniformly distributed grid. The finite difference discretization of the spatial derivatives leads to a system of semidiscrete ordinary differential equations:

$$\frac{\partial u_{ij}}{\partial t} = f(t, u_{ij}) + g(t, u_{ij}) \quad (14)$$

where $f(t, u_{ij})$ and $g(t, u_{ij})$ are the split nonstiff and stiff terms given by

$$f(t, u_{ij}) = \left\{ -\frac{\partial u}{\partial x} \right\}_{ij} \quad (15)$$

Table 2 Temporal accuracy of the LSSIRK-4A and LSSIRK-4C methods for explicit calculations

Δt	LSSIRK-4A		LSSIRK-4C	
	e_3	R_3	e_3	R_3
$h=0.0625$	$3.44E-5$	8.0	$9.59E-6$	8.2
$h/2$	$4.29E-6$	8.0	$1.18E-6$	8.1
$h/4$	$5.36E-7$	8.0	$1.46E-7$	8.1
$h/8$	$6.69E-8$	8.0	$1.82E-8$	8.0
$h/16$	$8.36E-9$	8.0	$2.27E-9$	8.0
$h/32$	$1.04E-9$	8.0	$2.83E-10$	8.0
$h/64$	$1.31E-10$	8.0	$3.53E-11$	8.0

$$g(t, u_{ij}) = \left\{ -\frac{\partial u}{\partial y} + \frac{1}{R} \frac{\partial^2 u}{\partial y^2} + G(x, y, t) \right\}_{ij} \quad (16)$$

Explicit third-order upwind discretization is used for the discretization of the term u_x , whereas the fourth-order central difference approximations are used for the discretization of the u_y and u_{yy} terms. Special treatments are needed for the discretization at grid points near the upper and lower boundary points. We use fourth-order extrapolation at the walls and periodic boundary conditions in the x direction. The spatial discretization leads to a system of nonautonomous split ordinary differential equations, which is advanced in time by using the new third-order LSSIRK-4C scheme. The $f(t, u_{ij})$ term is treated explicitly, and the $g(t, u_{ij})$ is treated implicitly.

The specific conditions used in the computations are $R = 10$ and $k = 0.01$. The solutions are obtained by using a set of 51×21 uniform grid points. The numerical solutions obtained by using the LSSIRK-4C scheme are compared with the analytical solution. Figure 1 shows the comparison of the contours of $u(x, y, t)$ of the numerical simulation and the exact solution at time $t = 0.702824$. These contour plots of $u(x, y, t)$ show three peaks in x and y with nearly identical values for both the result of LSSIRK-4C and the analytical solution. More detailed comparisons are made for the comparison of the two solutions in variations in the x and y directions. Figure 2 shows a comparison of the distribution of the solutions $u(x, y, t)$ in the y direction along the $x = 0$ line at $t = 0.702824$. Figure 3 shows a similar comparison of the distribution in the x direction along the $y = 0.88$ line at $t = 0.702824$. The results show that the third-order LS Runge–Kutta scheme produces very accurate results

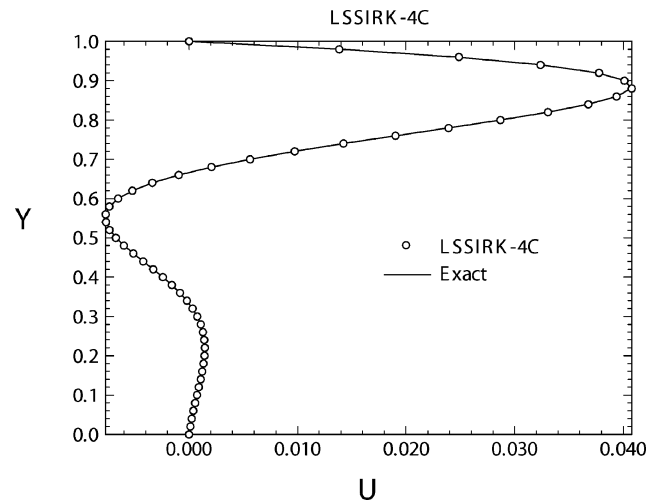


Fig. 2 Distribution of transient solution in y direction at $x = 0$ and $t = 0.702824$.

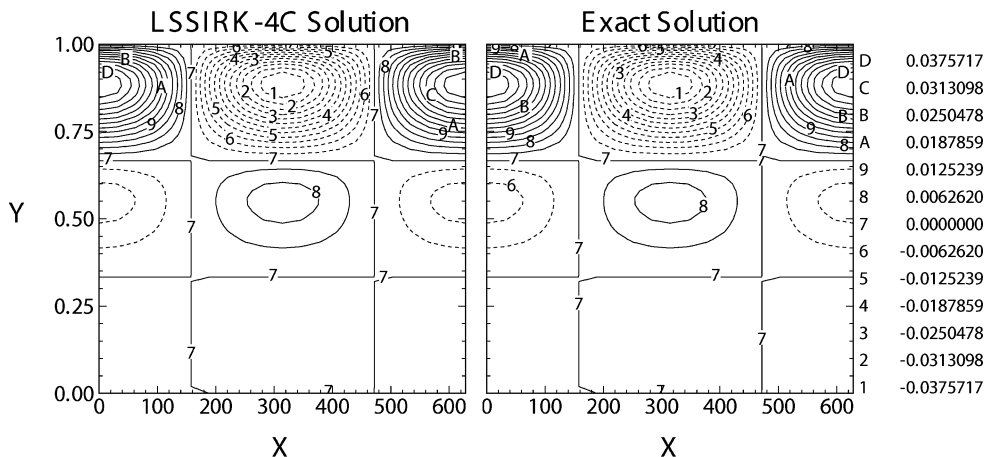


Fig. 1 Contours of decaying solution at time $t = 0.702824$.

Table 3 Temporal accuracy of the LSSIRK-4C on the stiff convection–diffusion problem at $t = 0.0878531$, $x = 0$, and $y = 0.84$

Δt	L_1^a	e_3^b	R_3
$h = 0.439265D-2$	$5.65E-4$	$4.50E-4$	6.6
$h/2$	$5.74E-4$	$6.82E-5$	7.9
$h/4$	$5.75E-4$	$8.67E-6$	7.9
$h/8$	$5.75E-4$	$1.09E-6$	8.0
$h/16$	$5.75E-4$	$1.37E-7$	8.0
$h/32$	$5.75E-4$	$1.72E-8$	8.0

^a L_1 -norm error. ^bNumerical error based on the extrapolation.

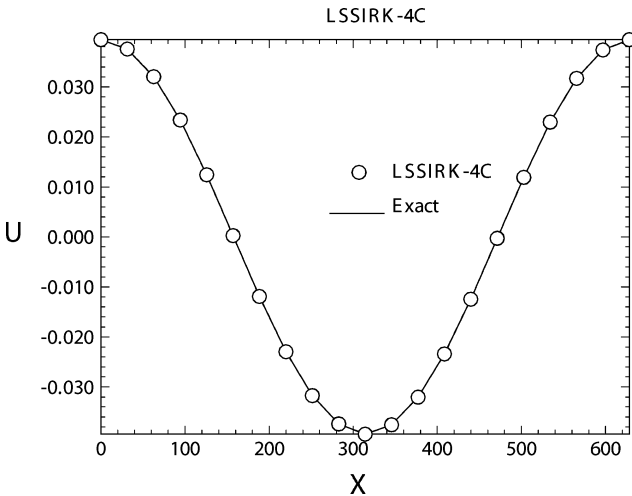


Fig. 3 Distribution of transient solution in x direction at $y = 0.88$ and $t = 0.702824$.

in predicting the transient behavior of a stiff nonautonomous convection–diffusion model problem.

The temporal accuracy of the computations using the LSSIRK-4C scheme is evaluated by a temporal grid refinement study. Here, both the L_1 error and the numerical error based on the Richardson extrapolation are computed. Table 3 summarizes those computed values at each refined grid. The results in the table show that the linearized low-storage method is third-order.

Stiff Partial Differential Equations

In this section, the new hybrid Runge–Kutta schemes are tested through two very stiff model partial differential equations. The first case is a stiff relaxation model equation discussed in Ref. 2. The second case is a system of partial differential equations with a stiff source term.³ The performance of the SIRK-3C scheme in computing these two stiff equations is compared with that of the time-splitting methods in solving stiff equations involving both sharp and smooth wave propagation.

The time-splitting or the fractional-stepping methods can achieve a second-order accuracy in time integration in solving partial differential equations with stiff source terms.^{4,5} Applying the Strang splitting⁶ to maintain a second-order accuracy, the solution at time $n + 1$ is given as

$$u^{n+1} = \mathcal{L}_g(h/2)\mathcal{L}_f(h)\mathcal{L}_g(h/2)u^n \quad (17)$$

where \mathcal{L}_f is the explicit temporal operator to integrate the partial differential equation without the source term and \mathcal{L}_g is the implicit temporal operator to integrate stiff source term only. The spatial accuracy is related to the choice of spatial discretization schemes used in \mathcal{L}_f . In the current analysis, the third-order essentially nonoscillatory (ENO)–Roe scheme with sharpening (ENO–Roe–S-3) by Shu and Osher⁷ with the shock-sharpening mechanism⁸ is used in calculating the convective flux term. The time advancement in the time-splitting scheme is achieved by using an explicit third-order Runge–Kutta scheme.

On the other hand, the SIRK-3C scheme treats the flux discretization $f(u)$ explicitly and the source term $g(u)$ implicitly in the same stage. Here, $f(u)$ is discretized using the same third-order ENO–Roe–S scheme as in the time-splitting case. The results of the SIRK-3C scheme are compared with those of the time-split scheme for computing two partial differential equations with stiff source terms.

Stiff Relaxation Model Equation

The first equation with stiff source term is a linear advection model equation discussed in Ref. 2, that is,

$$u_t + u_x = S(u) \quad (18)$$

where

$$S(u) = -\mu u(u - 1)\left(u - \frac{1}{2}\right) \quad (19)$$

This linear advection equation with the source term is stiff for large μ . The equation has two stable equilibria at $u = 1$ and 0 and an unstable equilibrium point at $u = \frac{1}{2}$. The stiffness of the equation is characterized by a stiffness parameter defined by $k\mu$, where k is the appropriate timescale of advection on the grid. This stiffness parameter is called the cell Damköhler number, which is a ratio of advection timescale h to the relaxation timescale for the source term, namely $1/\mu$. For a large value of $k\mu$ and arbitrary initial data, the solution rapidly approaches the upper equilibrium if initial $u(x_0, 0) > \frac{1}{2}$ and the lower equilibrium at $u(x, t) = 0$ if $u(x_0, 0) < \frac{1}{2}$.

Model equation (18) is computed by using the third-order SIRK-3C after the convection term is discretized by the ENO–Roe–S-3 scheme. The results of the SIRK-3C scheme is compared with the exact solution. Because the time-splitting method has been a standard method for stiff ordinary differential equations, the results of the time-splitting method with the same spatial ENO–Roe–S-3 scheme for the convection term are also presented for comparison.

The robustness of the SIRK-3C scheme is first tested by Eq. (18) with very large stiffness parameter $k\mu$. The initial condition of the computations is given by the piecewise constant data,

$$u(x, 0) = \begin{cases} 1 & \text{if } x < 0.3 \\ 0 & \text{if } x > 0.3 \end{cases} \quad (20)$$

and the stiffness parameter $k\mu$ is much larger than 1. The exact solution is a propagating step function. The solution is obtained by using a 50-point uniform grid. Figure 4 shows a comparison of two results obtained by SIRK-3C and the time-splitting scheme. The results show that the two methods become nearly identical when stiffness is reduced to zero as in case $k\mu = 0$. This adds to the observation that approximately one cell is used to capture a shock after applying the subcell resolution during the ENO stage. When the stiffness is large such that the cell Damköhler number becomes much greater than 1, the prediction of shock location by all methods starts to fail. In fact at a highest stiffness, $k\mu \geq 15$, the discontinuity does not propagate at all for the SIRK-3C calculations, whereas an incorrect prediction of the location of discontinuity is observed in the Strang⁶ time-splitting calculations. This degrading feature of precisely predicting shock locations at high stiffness is a resultant of the underprediction of small timescale, which allows the points within discontinuity to get turned on incorrectly. However, the time-splitting method has shown its robustness with a slight overprediction of exact shock location even when the system stiffness approached its asymptotic limit.

The accuracy of the SIRK-3C schemes in computing stiff convection equation with source term is also tested in computing the solution of Eq. (18) for the case of smooth initial conditions. The initial condition consists of small perturbations around the value of the solution at one of three equilibrium states. The subsequent evaluation of the solution can be described by a linearized perturbation solution of Eq. (18). The exact solutions of the linear evaluation are used to compare the numerical solutions. The model equation of nonhomogeneous convection equation (18) has three points of

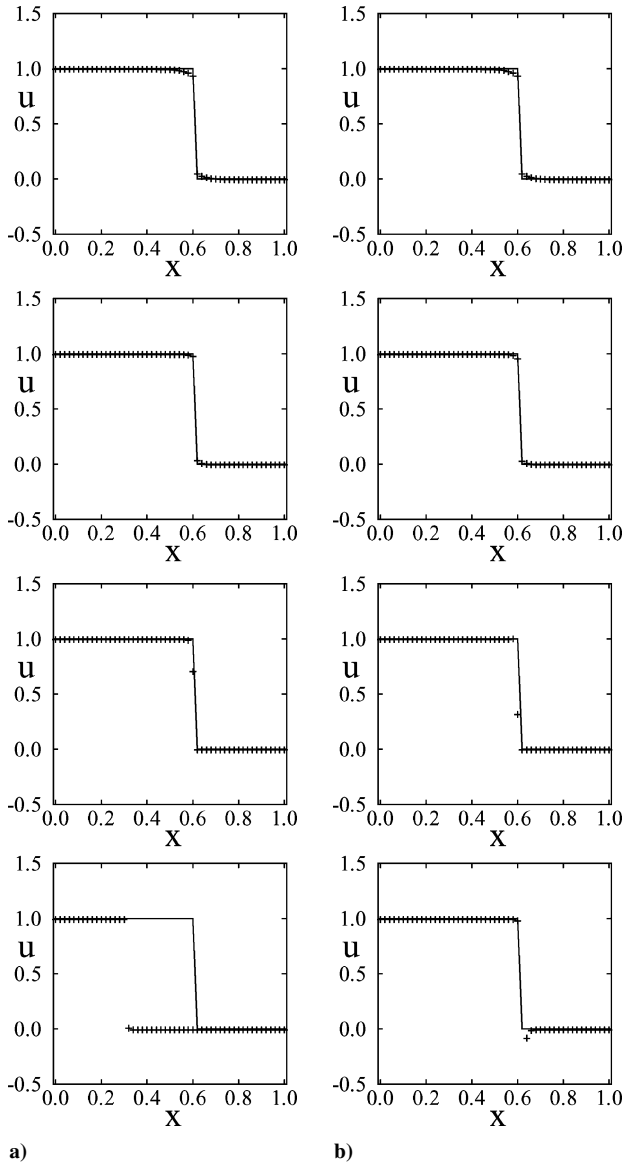


Fig. 4 Numerical results using a) SIRK-3C with ENO-Roe-S-3 and b) time splitting with ENO-Roe-S-3/RK-3. The cell Damköhler numbers are $k\mu = 0, 0.15, 1.5$, and 15 , increasing from top to bottom: —, true solution and +, computed solution.

equilibria as mentioned earlier. We assume the solution is a linear perturbation from the first equilibrium point in the following form:

$$u(x, t) = 1 + \varepsilon u'(x, t) \quad (21)$$

where the perturbation parameter ε is a small number (usually less than 10^{-3}) and $\varepsilon u'$ is the small perturbations of u with respect to the equilibrium points. Substituting Eq. (21) into Eq. (18) leads to the following linearized equation for the perturbation:

$$u'_t + u'_x = -\mu(u'/2) \quad (22)$$

For an initial condition of $u'(x, t) = \varepsilon \cos(\alpha x)$, the exact solution of the linearized equation is obtained,

$$u(x, t) = 1 + \varepsilon \exp[-(\mu/2)t] \cos[\alpha(x - t)] \quad (23)$$

Figure 5 shows a comparison of the analytical solution with the numerical solution by the SIRK-3C scheme at time $t = 0.09375$ when $u = 1 + \varepsilon \cos \alpha x$ is used as initial data. Because the solution has a smooth spatial distribution, we use a third-order explicit upwind scheme to discretize the spatial derivative term u_x :

$$\frac{\partial f(u)_j}{\partial x} = \frac{f(u)_{j-2} - 6f(u)_{j-1} + 3f(u)_j + 2f(u)_{j+1}}{6\Delta x} \quad (24)$$

Table 4 Numerical errors with $\mathcal{D} = 30$ and $h/\Delta x = 0.75$

Case	SIRK-3C		Time split	
	L_∞	R_3	L_∞	R_2
h	0.178×10^{-8}		0.108×10^{-7}	
$h/2$	0.221×10^{-9}	8.05	0.248×10^{-8}	4.37

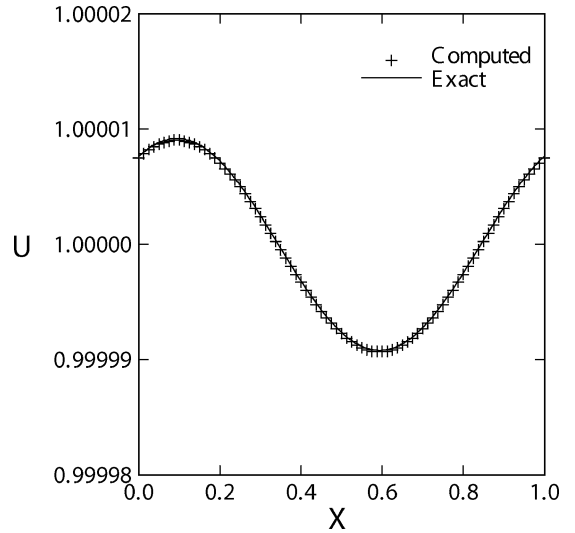


Fig. 5 Numerical result using SIRK-3C with third-order explicit upwind scheme; no visible discrepancy in the propagation of a sinusoidal wave of length one at a moderate stiffness ($\mathcal{D} = 30$): —, analytical solution at small ε and +, computed solution.

Periodic conditions are enforced on the boundaries of a computational domain of a single wave length. The period of a unity is used for the wave. A convenient parameter of the system stiffness, the Damköhler number \mathcal{D} is defined as the ratio of the fluid timescale to the reaction timescale. A period of 1 is taken as the fluid timescale, whereas $2/\mu$ is the representative reaction timescale:

$$\mathcal{D} = t_{\text{fluid}}/t_{\text{reaction}} = 1/(2/\mu) \quad (25)$$

For the solution in Fig. 5, this Damköhler number and the Courant–Friedrichs–Lewy number are kept at 30 and 0.75, respectively, allowing relatively large time step h . Figure 5 shows a very good agreement of the analytical solution with the numerical solution by the SIRK-3C scheme.

The temporal orders of accuracy of the SIRK-3C and time-splitting schemes are evaluated again by a grid refinement study. Table 4 summarizes the L_∞ -norm error computed by the two methods. The error ratios in Table 4 show that the schemes are third-order accurate in time for the SIRK-3C method and second order for the time-splitting method. The computed error ratios when the h is halved to $h/2$ should become $R = 2^p$ for a p th-order scheme. With the magnitude of L_∞ -norm error nearly 11 times greater than that of the SIRK-3C, the time-splitting scheme has its errors mainly evolved from the temporal accuracy. This is an expected behavior of a second-order scheme that, when Δx is reasonably small, the effect of temporal accuracy is significant in total error, suggesting the advantage of the third-order SIRK-3C scheme in computing transient smooth solutions of stiff equations.

System of Stiff Partial Differential Equations

The SIRK-3C scheme is tested in the following system of partial differential equations with a stiff source term³:

$$\frac{\partial v}{\partial t} + \frac{\partial w}{\partial x} = 0 \quad (26)$$

$$\frac{\partial w}{\partial t} + \frac{\partial}{\partial x} \left(v + \frac{1}{2}v^2 \right) = -10^8 \left(w - \frac{1}{2}v^2 \right) \quad (27)$$

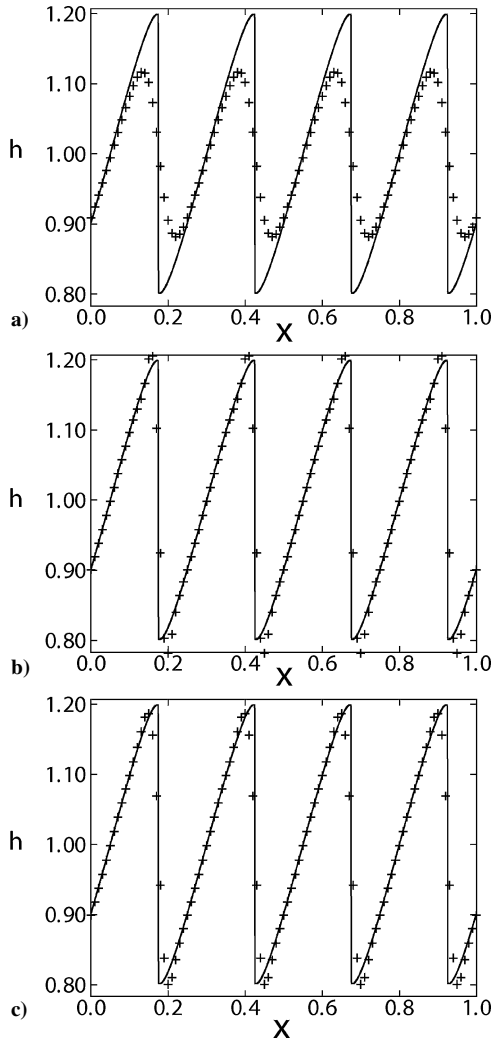


Fig. 6 Numerical results using a) Strang splitting, b) second-order splitting, and c) SIRK-3C with $\mu = 10^8$ and $t = 0.3$: —, exact solutions and +, numerical solutions.

with initial conditions

$$v(x, 0) = 1 + 0.2 \sin(8\pi x) \quad (28)$$

$$w(x, 0) = \frac{1}{2}v(x, 0)^2 \quad (29)$$

This is a 2×2 system of partial differential equations. The equation has a very large stiffness parameter, that is, the Damköhler number is on the order of 10^8 .

The equations are computed by the SIRK-3C, the Strang⁶ time-splitting, and the second-order-splitting⁹ schemes for comparison. Figure 6 shows a comparison of the numerical solutions of the SIRK-3C, second-order time-splitting, and Strang time-splitting schemes for solution at time $t = 0.3$. In the computations, the spatial resolution is fixed at a uniform grid size of 10^{-2} , whereas the temporal increment is chosen at $h = 0.005$. It is found that all three schemes show very good stability in solving the very stiff equation. On the other hand, the results of the second-order splitting show a noticeable improvement in accuracy over those obtained from Strang time-splitting scheme. However, the solution of the second-order splitting still overshoots at the locations of complicated structures. From this exercise, the SIRK-3C scheme seems suitable for computing the stiff equations with small-scale structures, which is the case for many reactive flow problems.

Steady and Unsteady Combustion Flows

Three test cases of one and two dimensional detonations with hydrogen–air mixture are simulated using the new SIRK schemes

in this section. The three test cases are 1) one-dimensional unsteady reacting shock propagation, 2) steady two-dimensional detonation flow over a wedge, and 3) unsteady propagation of two-dimensional detonation waves in a channel.

The governing equations for reacting flows are the Euler equations with nonequilibrium chemistry and vibrational energy mode. They are

$$\frac{\partial \mathbf{U}}{\partial t} + \frac{\partial \mathbf{F}_j}{\partial x_j} = \mathbf{W} \quad (30)$$

where

$$\mathbf{U} = \begin{bmatrix} \rho_1 \\ \vdots \\ \rho_m \\ \rho u_1 \\ \rho u_2 \\ \rho u_3 \\ e \\ e_v \end{bmatrix}, \quad \mathbf{W} = \begin{bmatrix} \dot{w}_1 \\ \vdots \\ \dot{w}_m \\ 0 \\ 0 \\ 0 \\ 0 \\ \dot{w}_v \end{bmatrix} \quad (31)$$

$$\mathbf{F}_j = \begin{bmatrix} \rho_1 u_j \\ \vdots \\ \rho_m u_j \\ \rho u_1 u_j + p \delta_{1j} \\ \rho u_2 u_j + p \delta_{2j} \\ \rho u_3 u_j + p \delta_{3j} \\ (e + p)u_j \\ e_v u_j \end{bmatrix} \quad (32)$$

The equation of state for pressure is given by Dalton's law for a mixture of thermally perfect gases,

$$p = \rho RT = \sum_i^m \rho_i R_i T \quad (33)$$

where R_i is the species specific gas constant. The total energy is defined as

$$e = \sum_{i=1}^m \rho_i c_{vi} T + e_v + \rho \frac{1}{2} u_k u_k + \sum_{i=1}^m \rho_i h_i^0 \quad (34)$$

where h_i^0 is the species heat of formation. The specific heat at constant volume c_{vi} is equal to $3R_i/2$ and $5R_i/2$ for monatomic and diatomic species and $6R_i/2$ for other atomic species. To account for the vibrational nonequilibrium, the thermal state of the gas is described by two separate and independent temperatures. One temperature T represents the translational and rotational modes of molecular energy, whereas the other temperature T_v represents the energy stored in the vibrational degrees of freedom of the molecules. This approach requires a separate energy equation for vibrational energy and allows an harmonic oscillator model to be used to represent the energy in the vibrational modes. It is assumed that the anharmonic effects and the excitation of electronic states are not important for the flow of interest. The vibrational source term \dot{w}_v is defined in Ref. 10.

The full reaction mechanism for modeling a hydrogen–air combustion is the 9-species, 48-step model of Oran et al.¹¹ The dissociation of N_2 is neglected because all of our combustion applications described in this paper occur below the temperature 3500 K and pressure 27 atm, above which the dissociation may become more significant.

Table 5 Parameters for the strong ignition simulation

Parameter	Undisturbed	Incident	Reflected
T , K	298.0	621.0	1,036
P , Pa	6687.45	36,670.6	131,722.5
u_{fluid} , m/s		465.4	
u_{shock} , m/s		756.1	450

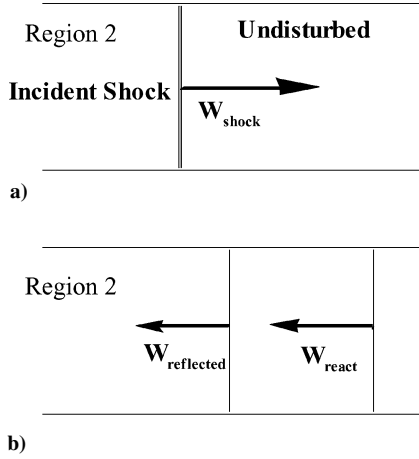


Fig. 7 Schematic of geometry used in the shock tube calculations, $W_{\text{shock}} > W_{\text{react}} > W_{\text{reflected}}$: a) incident shock of speed W_{shock} traveling to the right and reflected at the wall and b) propagation of the reaction wave into region 2 in later time.

One-Dimensional Shock Reflection in a Shock Tube

The process of a shock wave reflection from a rigid wall is simulated for reactive gas of hydrogen–oxygen–argon mixtures in a shock tube. Figure 7 shows a schematic of the shock tube, where incident shock is reflected and then followed by a reacting shock. The reactive wave will eventually catch up with the reflecting shock and become a transmitted detonation. The flow conditions are the same as those used in shock tube experiments performed by Cohen and Larsen¹² and numerical simulation by Oran et al.¹¹ using flux corrected transport (FCT) method with adaptive mesh refinement (AMR). A detailed 48-step chemical reactions mechanism with 9 species¹¹ is used in our simulation. The initial mixture consists of H_2 , O_2 , and Ar with 2:1:7 in moles. The conditions in each region are listed in Table 5.

A coarse grid of 100 cells with uniform spacing ($\Delta x = 0.12$ cm) is used in the current simulation. The results agree well with both the numerical results of Oran et al.¹¹ using finer grid ($\Delta x = 0.035$ cm) and the experimental results of Cohen and Larsen.¹² Figure 8 shows an $x - t$ plot of all three cases, where the wall is on the high side. Relative to the point at which the transmitted detonation wave is formed (approximately at $t = 260 \mu\text{s}$), two additional snapshots were taken to observe the before and after behavior of reflected-reacting shocks and transmitted detonation-contact discontinuity. Figures 9 and 10 show comparisons of the instantaneous temperature distributions at two time snapshots for SIRK-3C and FCT results. In Fig. 9, the waves are traveling to the left. The SIRK-3C results show a good agreement with the reported FCT results.¹¹ All of the pertinent flow structures as reported by Oran et al. are observed, and in particular a reflected expansion wave and a contact discontinuity are well observed in the flow behind a transmitted detonation.

Two-Dimensional Standing Oblique Detonation Wave over a Wedge

The second test of SIRK-3C scheme is a simulation of steady standing oblique detonation wave over a sharp wedge. The computational domain used in the two-dimensional detonation problem is shown in Fig. 11. For the simulation of supersonic premixed flow over a wedge at an angle θ , the incoming flow on the left boundary is at angle θ to the domain such that a uniform grid can be used. The particular test of the two dimensional standing oblique detonation with fast ignition is studied in Ref. 13. The freestream conditions are

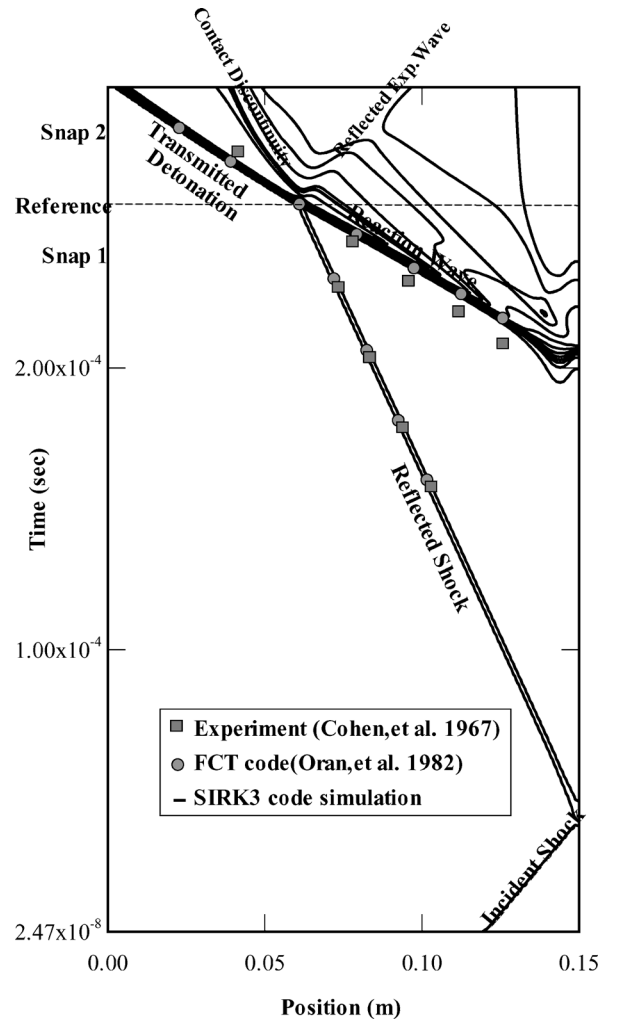


Fig. 8 Calculated temperature contour, showing the position of the reflected shock front, reactive wave, transmitted detonation, contact discontinuity, and reflected expansion wave as a function of time.

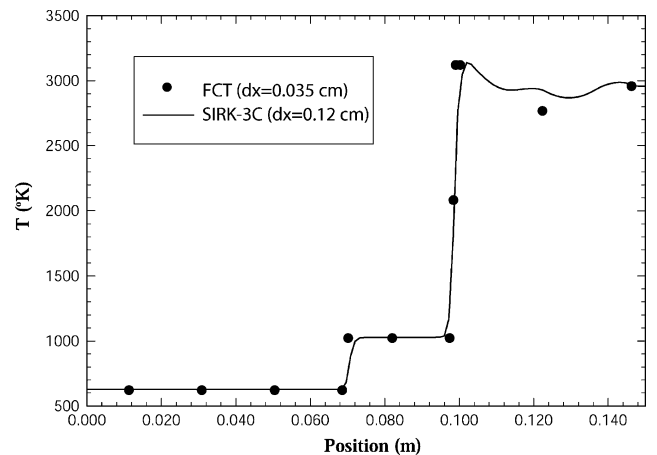


Fig. 9 Snapshot1: calculated temperature profile at time $239 \mu\text{s}$ before reacting wave catching up with reflected shock.

$M_{\infty} = 3.8$, $T_{\infty} = 840$ K, $P_{\infty} = 0.06$ atm, and wedge angle of 31 deg. The freestream is a mixture of $\text{H}_2:\text{O}_2:\text{N}_2 = 0.201:0.168:0.631$ by mass. The dimensions of the system are 28×10 cm. In the current simulation, a set of 50×75 points is used in the x and y directions, respectively. The mixture of 60% stoichiometry and the initial conditions as specified can ignite the fuel instantaneously, resulting in formations of coupled shocks and oblique detonations on a 31-deg wedge. In this case, we again use the detailed reaction mechanism

in Ref. 11 to model the finite-rate chemical reaction associated with the hydrogen–air premixed fuel combustion. The third-order ENO scheme⁷ is used to discretize the convection terms, whereas the time advancement is handled by the SIRK-3C scheme.

Figure 12 shows the temperature and pressure contours. The ignition temperature of the mixture is around 1000 K, so that the high freestream temperature drives the shock–detonation coupling at a supersonic speed with $M = 3.8$. Figure 13 shows a pressure distribu-

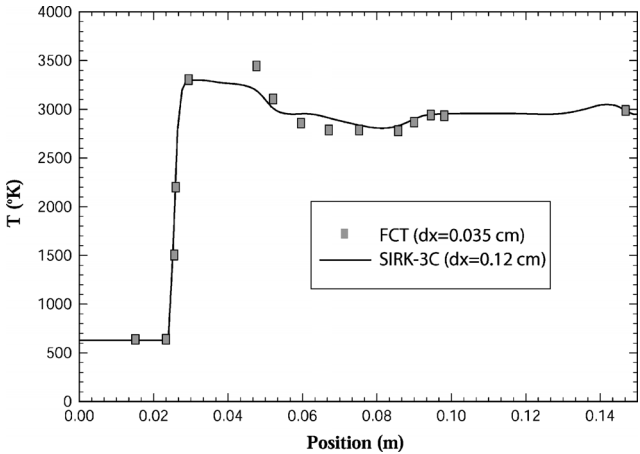


Fig. 10 Snapshot2: calculated temperature profile at the time 284 μ s when the transmitted detonation, contact discontinuity, and reflected expansion wave are observed.

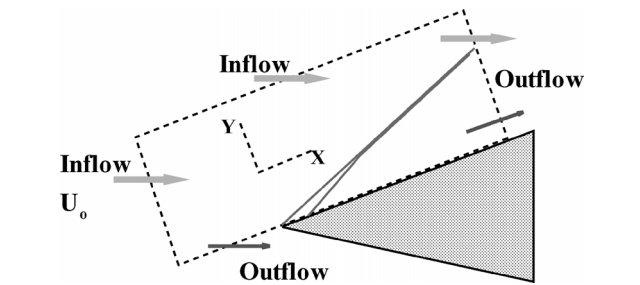


Fig. 11 Schematic of computational domain attached to the wedge surface.

tion along the cut made at a line of $y = \text{const}$. A slightly different cut was chosen in Ref. 13, but profiles obtained in our simulation agree reasonably well with the experimental results. The model for the relaxation rates plays an important role in the results. In the current simulation, a 48-step combustion mechanism was considered and third-order accuracy in time and space was achieved. The simulated flow structures are in quantitative agreement with those observed in experiments.

Two-Dimensional Unsteady Detonation Waves with Regular Cell Structures

The two-dimensional unsteady detonation wave with regular cell structures is simulated next. Detonation waves are multidimensional and unstable phenomena as demonstrated by the early experiments of Urtiew and Oppenheim.¹⁴ Existence of the triple points,¹⁵ consisting of an incident shock, a reflecting shock, and a Mach stem, is the main characteristic of reacting region behind the propagating shock front, and these detaching triple points from the leading front further contribute to the rolling up of vortices of opposite strength (Fig. 14). One distinctive feature of the instability process observed in experiments is the formation of regular cell structures as triple points collide as they come together in the incident shock and move away from each other in the newly formed Mach stem.

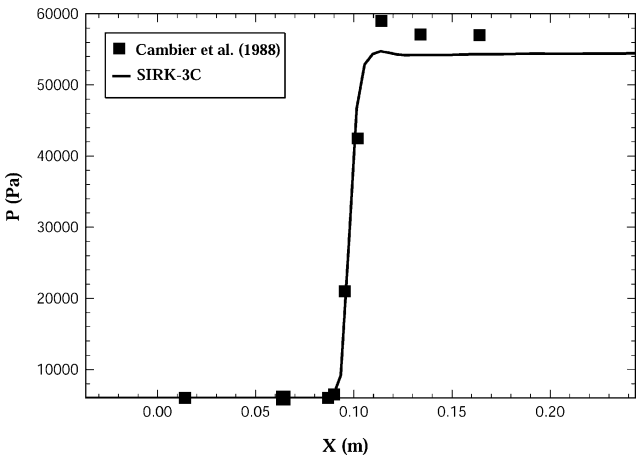


Fig. 13 Calculated pressure profile along the cut at grid row 32.

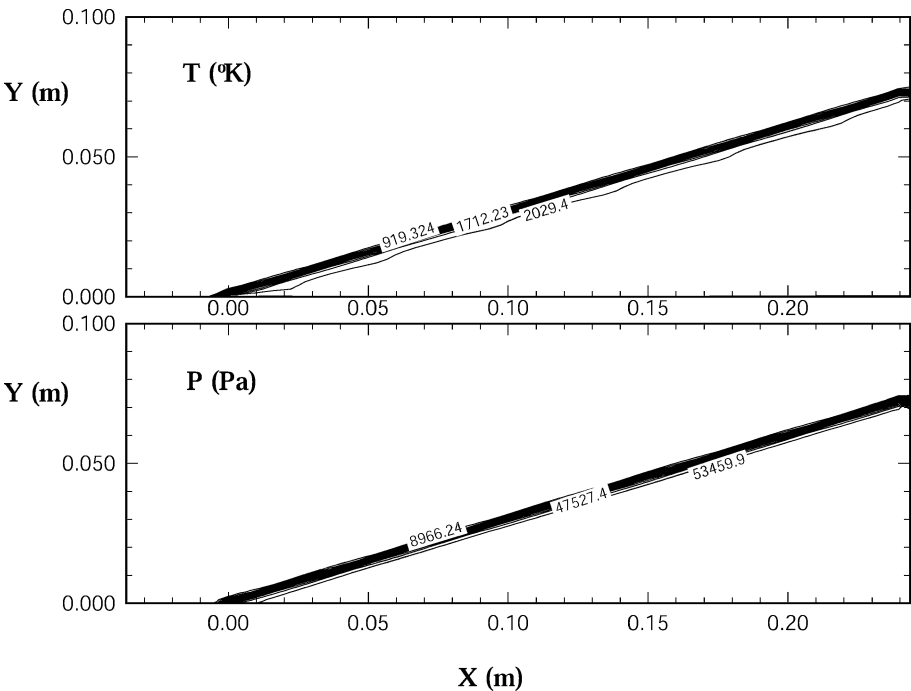


Fig. 12 Temperature and pressure contours for a supersonic reactive flow over a 23-deg wedge.

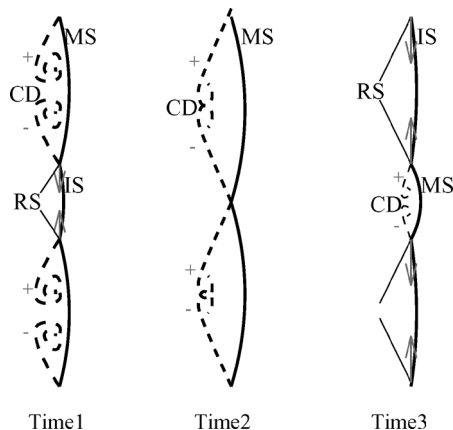


Fig. 14 Schematic of triple points movements just before the triple-points collision at Time1, at collision in Time2, and after the triple-points collision at Time3: rollup vortices of opposite direction are found behind the Mach shocks (MS), whereas reflected shocks (RS) are impinged on the incident shock (IS) at triple points.

To simulate the propagating two-dimensional detonation down the channel, we first consider the combustion of premixed fuel mechanism. The reaction is modeled by two species with a one-step $R \rightarrow P$ irreversible reaction represented by the Arrhenius kinetics. In this model, reactant is converted to product by a single-step irreversible chemical reaction, governed by Arrhenius kinetics. The specific heat ratio γ is fixed at 1.2, and a dimensionless parameter Q^+ is also introduced for the specific heat of formation. The specific total energy is

$$e/\rho = p/\rho(\gamma - 1) + (u^2 + v^2)/2 + Q^+ ZRT_0 \quad (35)$$

where Z is used to represent the reactant mass fraction, namely, the ratio of ρ_1 to ρ total. T_0 is the unreacted flow temperature. From this formulation of total energy, the temperature can be obtained by replacing p/ρ with RT such that the temperature T can be solved once all other values are computed from the numerical conservative value e . The case of one-step $R \rightarrow P$ irreversible reaction can be represented by the Arrhenius kinetics such that

$$\dot{w}_1 = -K \rho_1 \exp[(-E^+ T_0)/T] \quad (36)$$

$$\dot{w}_2 = 0 \quad (37)$$

where E^+ is the activation energy parameter and T_0 is the initial temperature of the unreacted gas mixture.

In the simulation, the initial data consist of the theoretical Zeldovich–von Neumann–Doering (Z–N–D) profiles on which a transverse perturbation is added to excite a fully multidimensional instability. If no transverse gradient is present in the initial data, the one-dimensional profile will be preserved such that only a longitudinal instability, if it exists, can be observed. A small sinusoidal perturbation of the form $u = \bar{u}[1 + \epsilon \sin(8\pi y)]$ is prescribed on the front of the wave, and alternatively each fluid variable in the Chapman–Jouguet states can be perturbed in a similar manner. The following is a description of the Chapman–Jouguet states used as initial data in the present simulation. The overdrive parameter f , which is defined as the square of the ratio of the detonation propagation velocity to the Chapman–Jouguet (C–J) velocity, $f = (D/D_{CJ})^2$, is held at 1.2. Erpenbeck¹⁶ gives one possible form for this C–J detonation speed:

$$D_{CJ} = \sqrt{1 + Q^+(\gamma^2 - 1)/2\gamma} + \sqrt{Q^+(\gamma^2 - 1)/2\gamma} \quad (38)$$

where Q^+ is also a known parameter. Once D_{CJ} is known, the initial inflow speed D can be set accordingly. Table 6 describes the C–J states.

The governing partial differential equations are the two-dimensional Euler equations with source term representing the rate of chemical reaction. The third-order ENO scheme is used to discretize the convective term, whereas the third-order SIRC-3C scheme is used to advance the ordinary differential equations in tem-

Table 6 Flow conditions with C–J states

Condition	Burnt (postshock)	Unburnt (preshock)
T , K	$T_{CJ} = 2853$	298
P , Pa	$P_{CJ} = 116,717$	6666
u , m/s	$D = 1956.46$	0
γ	1.2	1.2

Table 7 Flow conditions for a computation with detailed model of chemical kinetics and thermophysics for $H_2:O_2:Ar/2:1:7$ two-dimensional detonation

Condition	Burnt (postshock)	Unburnt (preshock)
T , K	2300	298
P , Pa	304,000	6666
u , m/s	1618	0
γ	1.556	1.556

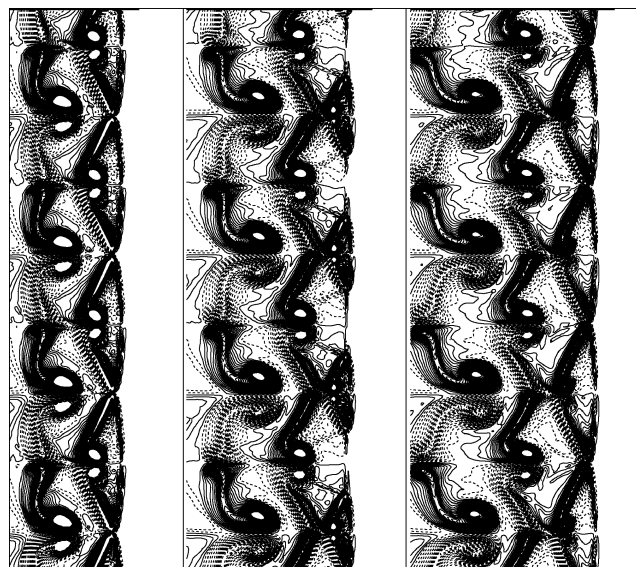


Fig. 15 Sequence in time of three snapshots of vorticity for the flow-field: $E^+ = 10$, $Q^+ = 50$, and $f = 1.2$.

poral steps. A set of uniform grids (300×300) was used in the physical domain of a 9 by 9 cm duct using periodic boundary conditions in the transverse direction. The nondimensionalized activation energy parameter E^+ is set at 10, and the heat release parameter Q^+ is specified at 50. The reaction coefficient K in Eq. (36) is chosen at 3.124.

Figure 15 shows a sequence of instantaneous vorticity contours of three moments in time. Figure 15 shows the evolving Mach structures and triple-point collisions that lead to the rolling up of vortex sheets, right after detaching from the triple points on detonation front. At a qualitative level, maximum vorticity peak-to-peak distance ratios are measured from the current results. They are within 6% of the reported results of Ref. 17. Figure 16 shows a time sequence of density contours in which the regular cell pattern behind the detonation front is observed. Again, the mushroomlike vortex structures are similar to those reported in Ref. 17.

The grid independence of the results are checked by simulating at a finer 600×600 grid. Figure 17 shows an instantaneous vorticity contours for the fine grid case. Compared with Fig. 15, the vortex structures of the two cases of different grids produce very similar cell vortex structures.

The results thus far are representative of an idealized multidimensional detonation involving one-step irreversible chemical reaction with two species. To test our scheme on a realistic reactive flow cases, we now consider a case of detailed H_2 – O_2 reaction mechanism for the two-dimensional detonation waves. Again, we use the detailed combustion model involving 48 reactions and 9 species.¹¹ The specific flow conditions of the multispecies, thermal and chemical nonequilibrium flow simulation are listed in Table 7.

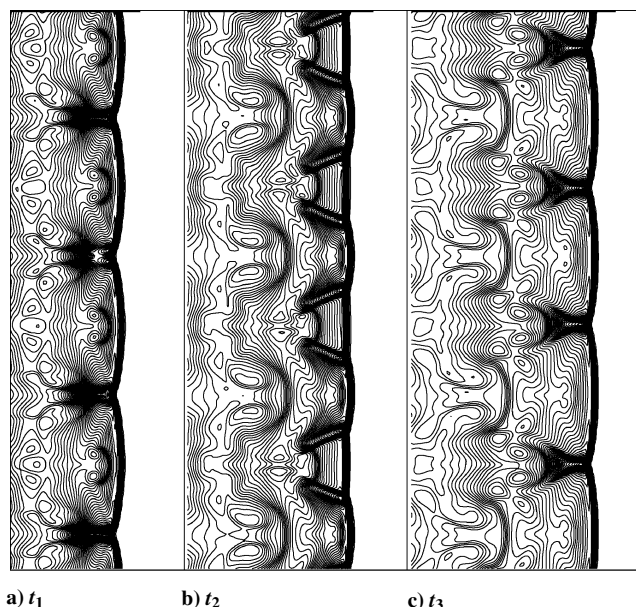


Fig. 16 Sequence in time of three snapshots of density for the flowfield: $E^+ = 10$, $Q^+ = 50$, and $f = 1.2$.



Fig. 17 Doubled grid result of vorticity field: $E^+ = 10$, $Q^+ = 50$, and $f = 1.2$.

In this simulation, 156 grids span a channel of width 4.68 cm, and one-dimensional reacting shock is initially perturbed to develop into unstable transverse detonation waves. Figure 18 shows the trajectories of triple points on pressure contours in the $y-t$ plane. The paths in the $y-t$ plane of triple point movements represent an approximate measure of the cell size and the cell reproduction time. It is a $y-t$ contour plot of pressure from which one can estimate the cell size corresponding to a combustion mixture used in a system. A typical one-cell size of hydrogen–air detonation is of order $10 \mu\text{s}$ (Ref. 18), and the observed size in the current simulation is approximately $38 \mu\text{s}$. The current numerical results are compared with the experimental results of Ref. 19 and other numerical results of Ref. 18. A good agreement with both experimental and other numerical results are observed for a cellular pattern characteristic of detonations in argon-diluted, low-pressure mixtures of hydrogen and oxygen. The

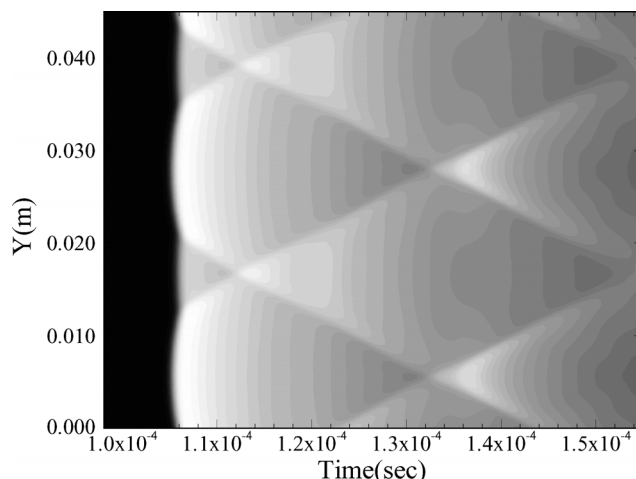


Fig. 18 Trajectories of triple points on pressure contours in $y-t$ plane.

triple point movement coincides with the reported results of Lefebvre et al.¹⁸ and computed cell size is also the same as that observed in the experiment. Only small discrepancies are noted in the computed average detonation speed, where the speeds are 1640, 1623, 1475, and 1619 m/s for the current Sirk-3C simulation, the computed value of Lefebvre et al.,¹⁸ the experimental value of Dormal et al.,¹⁹ and the calculated C–J detonation velocity,¹⁸ respectively. These small discrepancies are expected because of the complexity of the problem.

Conclusions

New hybrid Runge–Kutta schemes are shown to be high-order accurate and stable for solving stiff differential equations that model transient reacting flows. To illustrate this point, we have chosen LSSirk-4C to verify third-order accuracy and general Sirk-3C to reproduce numerical results of well-known dynamic shock and detonation problems.

The cost of running the new scheme is only a fraction of that needed to do a full implicit calculation. The elegant coupling between implicit and explicit Runge–Kutta methods removes the prohibitively small time-step requirement of solving stiff differential equations. Because of the LS framework, LSSirk schemes are suitable for large-scale computations requiring multiple arrays of data storage. Moreover, these Runge–Kutta-based hybrid solvers maintain high-order accuracy that is needed to track explicitly the widely varying timescales associated with numerical simulations of transients in reacting flows.

Acknowledgments

This research was supported by the Air Force Office of Scientific Research under Grant F49620-97-1-0030. The work was performed under the auspices of the U.S. Department of Energy by the University of California, Lawrence Livermore National Laboratory under Contract W-7405-Eng-48.

References

- Yoh, J. J., and Zhong, X., "New Hybrid Runge–Kutta Methods for Unsteady Reactive Flow Simulation," *AIAA Journal*, Vol. 42, No. 8, 2004, pp. 1593–1600.
- LeVeque, R. J., and Yee, H. C., "A Study of Numerical Methods for Hyperbolic Conservation Laws with Stiff Source Terms," *Journal of Computational Physics*, Vol. 86, 1990, pp. 187–210.
- Chen, G.-Q., Levermore, C. D., and Liu, T.-P., "Hyperbolic Conservation Laws with Stiff Relaxation Terms and Entropy," *Communications in Pure and Applied Mathematics*, Vol. 47, 1994, p. 787.
- Oran, E. S., and Boris, J. P., *Numerical Simulation of Reactive Flow*, Elsevier Science, New York, 1987.
- Yanenko, N. N., *The Method of Fractional Steps*, Springer-Verlag, 1971.
- Strang, G., "On the Construction and Comparison of Difference Schemes," *SIAM Journal on Numerical Analysis*, Vol. 5, 1968, pp. 506–517.

- ⁷Shu, C.-W., and Osher, S., "Efficient Implementation of Essentially Non-Oscillatory Schemes II," *Journal of Computational Physics*, Vol. 83, 1989, pp. 32–78.
- ⁸Harten, A., "High Resolution Schemes for Hyperbolic Conservation Laws," *Journal of Computational Physics*, Vol. 49, 1983, pp. 357–393.
- ⁹Jin, S., "Runge–Kutta Methods for Hyperbolic Conservation Laws with Stiff Relaxation Terms," *Journal of Computational Physics*, Vol. 122, 1995, pp. 51–67.
- ¹⁰Yoh, J. J., and Zhong, X., "Semi-Implicit Runge–Kutta Schemes for Stiff Multi-Dimensional Reacting Flows," AIAA Paper 97-0803, 1997.
- ¹¹Oran, E. S., Young, T. R., Boris, J. P., and Cohen, A., "Weak and Strong Ignition. I. Numerical Simulations of Shock Tube-Experiments," *Combustion and Flame*, Vol. 48, 1982, pp. 135–148.
- ¹²Cohen, A., and Larsen, J., U.S. Army Ballistics Research Lab., BRL Rept. 1386, Aberdeen, MD, 1967.
- ¹³Cambier, J., Adelman, H., and Menees, G. P., "Numerical Simulations of Oblique Detonations in Supersonic Combustion Chambers," *Journal of Propulsion*, Vol. 5, 1989, pp. 482–491.
- ¹⁴Urtiew, P. A., and Oppenheim, A. K., "Experimental Observations of the Transition to Detonation in an Explosive Gas," *Proceedings of the Royal Society of London, Series A: Mathematical and Physical Sciences*, Vol. 295, 1966, pp. 13–28.
- ¹⁵Fickett, W., and Davis, W. C., *Detonation*, Univ. of California Press, Berkeley, CA, 1979.
- ¹⁶Erpenbeck, J. J., "Nonlinear Theory of Unstable Two-Dimensional Detonation," *Physics of Fluids*, Vol. 13, 1970, pp. 2007–2026.
- ¹⁷Bourlioux, A., "Numerical Study of Unstable Detonations," Ph.D. Dissertation, Princeton Univ., Princeton, NJ, 1991.
- ¹⁸Lefebvre, M. H., Oran, E. S., Kailasanath, K., and Tiggelen, P. J. V., "The Influence of the Heat Capacity and Diluent on Detonation Structure," *Combustion and Flame*, Vol. 95, 1993, pp. 206–218.
- ¹⁹Dormal, M., Libouton, J. C., and VanTiggelen, P., "Evolution of Induction Time in Detonation Cells," *Acta Astronautica*, Vol. 6, 1979, p. 875.

C. Kaplan
Associate Editor